Full Paper

Propellants,
Explosives,
Pyrotechnics

Numerical Simulation for the Combustion of a Zirconium/Potassium Perchlorate Explosive inside a Closed Vessel

Doo-Hee Han,[a] Hong-Gye Sung,*[a] and Byung-Tae Ryu[b]

Abstract: The combustion of zirconium potassium perchlorate (ZPP) in a closed vessel is modelled and validated through a numerical simulation. Because the extremely high pressure oscillation occurs in less than a millisecond, an in-house computational fluid dynamics (CFD) code is used to observe the detailed flow structures and determine the adequate burning characteristics, including the burning rate. A hybrid RANS/LES scheme with a 5th order upwind weighted essentially non-oscillatory (WENO) is implemented to capture complex, strong shock waves in highly turbulent combustion. A two-way coupled Eulerian-Lagrangian scheme tracks the combusting ZPP granules reasonably well. Monodisperse and Rosin-Rammler assumptions are applied to the ZPP granule distribution. The monodisperse assumption reveals that the diameter of the ZPP (17 µm) achieves marginal agreement with the measurements. However, the Rosin-Rammler distribution improves the transient and dynamic combustion characteristics in that the small granules contribute to a faster burning rate and stronger shock waves. These results are more analogous to the closed vessel tests used as validation data.

Keywords: Closed vessel test · Zirconium potassium perchlorate (ZPP) · Reactive two-phase flow

1 Introduction

Zirconium potassium perchlorate is frequently used as a primary explosive for pyrotechnically actuated devices (PADs) due to its high-energy density, fast burning rate and easy ignition characteristics. It rapidly generates both hot gases and condensed combustion products, which serve as a driving force during combustion. PAD types include pin puller [1] and pyro valve [2], among others [3]. PADs are one-shot devices, but they can determine the success or failure of a mission. Thus, a malfunction or misfire is unacceptable. However, the uncertainty surrounding combustion characteristics and pyrotechnic shocks makes it difficult to guarantee success. A 1988 NASA report [4] identified 83 failures over 23 years with varying degrees of severity. Because pyrotechnic materials have very fast reaction rates, they release strong shock waves after ignition. The pyrotechnic shocks and vibrations depend on the shape of the device. It is possible to effectively dampen the intensity of a pyrotechnic shock by changing the vessel's shape or installing a small baffle. In this case, an effective numerical combustion model and CFD tool are required.

Gonthier et al. [5] and Jang et al. [6] fabricated a ZPP combustion model for a 0-D unsteady internal ballistics analysis. They modelled the ZPP combustion by dividing it with many granules and assuming that the granules burned at the surface regression rate. Their model achieved reasonable accuracy when considering its simplicity. However, because it was a 0-D model, it was not able to predict pressure oscillations. H. S. Lee [7] studied unsteady gas dynamic effects in a pyro device using 1-D internal ballistics. The

study could successfully calculate pressure oscillations. Buttigieg et al. [8] discovered the importance of the shock tube effect on devices. They concluded that the static pressure force by itself was not able to burst a closure. Rather, they asserted that the shock wave generated by the discharged gas was the important factor when designing a device. In terms of numerical simulations, A. Bougamra and H. Lu [9] conducted a CFD using ANSYS Fluent. They solved the Eulerian-Eulerian reactive two-phase flow for solid propellant combustion. However, their results did not contain any shock waves or oscillations. Balakrishnan et al. [10] used the reactive Eulerian-Lagrangian method to simulate burning aluminum in a post-detonation flow field. The burning aluminum was treated as a source term, and the complex Rayleigh-Taylor instability induced by the detonation was well captured with this method.

In this study, a numerical simulation for ZPP combustion inside a cylindrical closed vessel is conducted to analyze the detailed flow development and characteristics of the solid combustion. A cylindrical vessel is adopted rather than a spherical vessel to recreate more realistic PAD conditions; most PADs use cylindrical chamber configurations. In addi-

[a] *D.-H. Han, H.-G. Sung*
School of Aerospace and Mechanical Engineering
Korea Aerospace University
Deogyang-gu, Goyang-si, Gyeonggi 10540, Republic of Korea
*e-mail: hgsung@kau.ac.kr
[b] *B.-T. Ryu*
Agency for Defense Development
Yuseong-gu, Daejeon 34186, Republic of Korea

tion, cylindrical vessels are advantageous when validating the model because they experience distinct pressure oscillations. It is assumed that the pressed ZPP bed cracks into granules during ignition. The Lagrangian scheme tracks every ZPP granule in the combustion gas, while the Eulerian method solves the Navier-stokes equation for the combustion gas behavior. The average diameter of the ZPP granules is predicted by comparing the experimental data with the 0-D internal ballistics analysis. In addition, the effects of the initial granule size distribution are studied via the Rosin-Rammler equation.

2 Pyrotechnic Material and Test Apparatus for Validation

The pyrotechnic material consists of 52% zirconium, 42% $KClO_4$, 5% Viton B and 1% graphite by weight. The average diameter of the granules is 125 µm when manufactured, but they are pressed into a disk shape by applying 35 MPa of force before loading. They are then loaded into a metal holder, one side of which is blocked by an etching disk that can be ruptured. Electrically heated bridge wires are installed at the closed end to ignite the ZPP lump. Table 1 summarizes the ZPP properties. The combustion enthalpy was theoretically calculated, concerning initial composition and condition (P = 1 atm, T = 300 K). TMD denotes theoretical maximum density.

Table 1. Solid ZPP characteristics.

Parameter	Value	Unit
Combustion enthalpy	5750	J/kg
Theoretical Density	2440	Kg/m³
Burning rate constant, a	1.94×10^{-3}	$cm/ms/MPa^n$
Burning rate exponent, n	0.47	–
Loading density	0.51	TMD, %

Figure 1 illustrates the schematics of the experimental apparatus. This experiment is often called a closed vessel
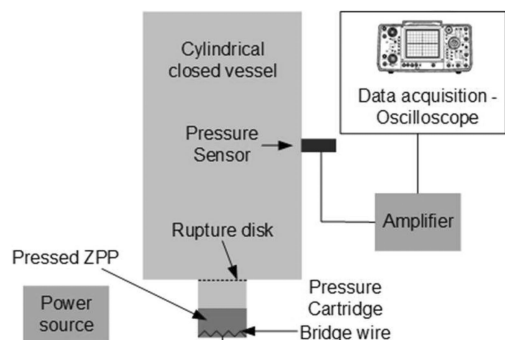

Figure 1. Schematic of closed vessel apparatus.

test or closed bomb test. It is widely used to test the performance of solid propellants [11, 12]. The holder containing the pressed ZPP lump, which is called the pressure cartridge, is installed at the bottom of the closed vessel. The bridge wire is installed in the pressure cartridge for ignition. It is electrically heated by a power source. The vessel is cylindrical with a 15-mm diameter and 55.2-mm height. The pressure sensor is installed in the middle of the vessel. The location of the sensor head diaphragm is aligned with the wall surface. A Kulite XTL-163-190-3000A pressure sensor is used. (This is a piezo resistance type sensor.) The signal generated by the sensor passes an amplifier and is collected using an oscilloscope with a sampling rate of 5 M/s. The test is carried out at the Hanwha Defense R&D Center [13].

3 Theoretical Model

3.1 Ignition and Combustion Modelling of Pressed ZPP Bed

Figure 2 displays a still image of the burning ZPP in an open space taken by a high-speed camera. When the bottom of the ZPP lump is ignited by the bridge wire, the rapidly generated internal pressure bursts the etching disk, and powder is dispersed into the available space. The discretely burning fire balls in the snapshot indicate that the ZPP lump has cracked into small granules after ignition.
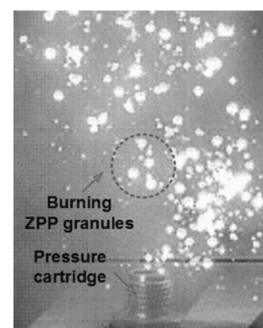
Figure 2. Snapshot of ZPP combustion in open space.

The total burning surface depends on the location of the bridge wire. If the ZPP bed is ignited at the open-end side, it will burn with a constant burning surface, which will be a cross sectional area of the lump. However, if the ZPP bed is ignited on the closed end side, the burning surface will increase significantly because the ZPP lump will crack into small granules, as seen in Figure 3. This figure depicts the conceptual burning surface modelling of a ZPP lump after closed end ignition. Figure 3 (a) shows the initial state of the pressed ZPP bed. In Figure 3 (b), the bridge wire is electrically heated and ignites the ZPP near the wire. This generates hot gases at high pressure. In Figure 3 (c), the hot
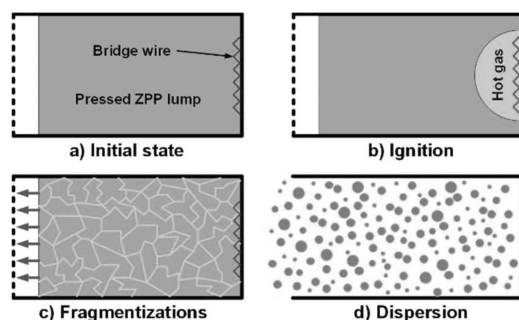
Figure 3. Ignition process of pressed ZPP lump in a pressure cartridge with bridge wire ignition.

gases pass through the pores of the ZPP bed and crack it into small granular shapes. Finally, in Figure 3 (d), the widened burning surface explosively generates high pressure, which bursts the etching disk. This enables the burning granules to disperse toward the closed vessel. In this case, the total burning surface can be modelled by predicting the average granule diameter or distribution of granule diameters.

The diameter distribution of dispersed ZPP granules is modelled using both the monodisperse assumption and the Rosin-Rammler distribution [14]. For the former, the total number of ZPP granules to be tracked can be attained using

$$N = M_t / (\pi d_{p.avg}^{3} / 6) \tag{1}$$

M_t is the total ZPP mass, and $d_{p.avg}$ is the average diameter of each ZPP granule. The total burning surface is given as

$$A_b = N \pi d_{p.avg}^{2} \tag{2}$$

With the Rosin-Rammler distribution, the number of particles and the burning area are different for every granule, and they depend on the distribution factor, k, and the average diameter, σ. The typical form of the Rosin-Rammler distribution is

$$\frac{M(d_{p.ind})}{M_t} = exp\left[-\left(\frac{d_{p.ind}}{\sigma}\right)^{k}\right] \tag{3}$$

$M(d_{p.i})$ is the cumulative mass of all granules greater then $d_{p.i}$. As k increases, the group of granules tends to form a narrower diameter distribution. The burning area is then

$$A_b = \sum_{ind=1}^{max} \pi d_{p.ind}^{2} \tag{4}$$

The burning rate of the granules is governed by the sur-

rounding pressure because it contains Viton B [15], which evaporates and emits hot gases. A stand-off distance exists from the granule surface to the flame zone. As the pressure increases, the stand-off distance decreases to promote the heat transfer rate from the flame zone to the surface. Therefore, each granule can be assumed to burn from its surface toward the core with a regression rate governed by the pressure. The pressure dependent regression rate is given by Vielle's law as

$$\dot{r} = a p^{n} \; [mm/s] \tag{5}$$

The regression rate constant, a, and exponent, n, are $1.94 \times 10^{-3} \; cm/ms/MPa^{n}$ and 0.47 [16], respectively. With the regression rate, the total reaction rate or mass generation rate of all the granules is given by

$$\dot{m}_{zpp} = A_b \dot{r} \rho_{zpp} \tag{6}$$

where ρ_{zpp} is the ZPP density. Finally, the total energy release rate during combustion can be obtained by multiplying the combustion enthalpy.

$$\dot{q}_{zpp} = \dot{m}_{zpp} h_{comb} \tag{7}$$

where the combustion enthalpy of the ZPP, h_{comb}, is 5750 J/kg.

The properties of the combustion product are obtained using the NASA CEA code [17] and NIST database [18]. The required properties are the specific heat, conductivity, viscosity and molecular weight. The ZPP combustion products are complex compositions of many species. Instead of solving the individual gas species during the calculation, the combustion products can be treated as a single gas species to increase computational efficiency. To do this, the representative values of the thermal and gas properties should be established. Table 2 shows the global reaction model for the ZPP using CEA at 3 MPa. The molecular weight, MW_{mix}, and specific heat at constant pressure, $c_{p.mix}$, of the combustion product can be calculated using Eqs. (8) and (10). The specific heat of each species is a polynomial function of temperature expressed as Eq. (9).

Table 2. Combustion products of ZPP at P = 3 MPa and T = 300 K.

Reactants (state, conc.)	Combustion products (state, concentration) Final temperature = 4578 K
Zr(s, 0.52) + KClO₄(s, 0.42) + Graphite (s, 0.01) + Viton b (s, 0.05)	ZrO₂(l, 0.481) + ZrO(g, 0.143) + KCl(g, 0.104) + KF(g, 0.075) + CO(g, 0.061) + Cl(g, 0.058) + ZrO₂(g, 0.047) + etc. (less than 1%)

$$MW_{mix} = \sum_{ind} Y_{ind} MW_{ind} \tag{8}$$

$$c_{p.ind} = a_{ind} + b_{ind}T + c_{ind}T^2 + d_{ind}T^3 + e_{ind}/T^2 \tag{9}$$

$$c_{p.mix} = \sum_{ind} Y_{ind} c_{p.ind} \tag{10}$$

Coefficients a_{ind}, b_{ind}, c_{ind}, d_{ind} and e_{ind} are the accessible via NIST database. Calculated coefficients for ZPP $c_{p.mix}$ are 47.0909, 0.30529, 0.17012, -0.01523 and 13.4635.

The constant conductivity and viscosity are used due to the lack of NIST data for all species. The CEA transport properties produce a conductivity value of 1.4714 W/m·K and viscosity value of 1.3885 millipoise.

3.2 0-D Unsteady Internal Ballistics Analysis

For simplicity, the model treats the thermal properties of the vessel as lumped parameters. The ZPP granules emit combustion products and energy. Equations (6) and (7) are used to calculate the product production rate and energy release rate. The combustion products are differentiated into gas and condensed phases because the condensed phase does not contribute to the pressure buildup process. The mass ratio of the gas and condensed phases is expressed as the mass fraction of the condensed combustion products (CCP).

$$\eta_{cp} = \frac{m_{cp}}{m_{gas} + m_{cp}} \tag{11}$$

The value of η_{cp} is obtained as a function of pressure using NASA's chemical equilibrium CEA code. The release rate of each phase can be expressed as

$$\dot{m}_{gas} = (1 - \eta_{cp})\dot{m}_{zpp} \tag{12}$$

$$\dot{m}_{cp} = \eta_{cp}\dot{m}_{zpp} \tag{13}$$

The Noble-Abel equation of state [19] for pyrotechnic combustion conditions in a closed vessel has been widely utilized because of its versatile application. Thus, the Noble-Abel EOS is derived to obtain the pressure slope equation.

$$\frac{dp}{dt} = \frac{\dot{m}_{gas}RT + mR\dot{T} + \dot{m}_{gas}pb - p\dot{V}}{V - M_{total}b} \tag{14}$$

The temperature slope is derived from the energy equation and expressed as

$$\frac{dT}{dt} = \frac{\dot{q}_{zpp} - \dot{m}_{zpp}c_pT - \dot{Q}_{loss}}{c_v M_{total}} \tag{15}$$

The values for R, c_p and c_v are obtained using CEA. A

more detailed description of the 0-D internal ballistics code is provided in Ref [1].

3.3 2-D Computational Fluid Dynamics with Particle Tracking Method

The computational fluid dynamics (CFD) is carried out using a compressible, reactive two-phase and multi-block in-house-code. The Eulerian-Lagrangian solver handles the coupled gas-particle flow. The Eulerian approach is suitable for the gas phase under the assumption that a continuum is present, while the Lagrangian approach locates and tracks particles in a domain with interpolated Eulerian fluid properties [20].

The finite volume method (FVM) is used to solve a 2-D fully compressible Navier-Stokes equation with species transportation using an in-house-code. Equations (16) to (19) represent the Eulerian governing equations of continuity, momentum, energy and species, respectively.

$$\frac{\partial \bar{\rho}}{\partial t} + \frac{\partial \bar{\rho}u_j}{\partial x_j} = \dot{\rho}_s \tag{16}$$

$$\frac{\partial \bar{\rho}\tilde{u}_i}{\partial t} + \frac{\partial \left(\bar{\rho}\tilde{u}_i\tilde{u}_j + \bar{p}\delta_{ij}\right)}{\partial x_j} = \frac{\partial \left(\tau_{ij} - \overline{\rho u_j'' u_i''}\right)}{\partial x_j} + \dot{F}_s \tag{17}$$

$$\frac{\partial \bar{\rho}\tilde{E}}{\partial t} + \frac{\partial \left(\left(\bar{\rho}\tilde{E} + \bar{p}\right)\tilde{u}_j\right)}{\partial x_j} = \frac{\partial \left(\bar{u}_i\bar{\tau}_{ij} - \overline{\rho h'' u_i''}\right)}{\partial x_j} - \frac{\partial \bar{q}_j}{\partial x_i} + \dot{Q}_s \tag{18}$$

$$\frac{\partial \bar{\rho}\tilde{Y}_k}{\partial t} + \frac{\partial \left(\rho\tilde{u}_j\tilde{Y}_k\right)}{\partial x_j} = \frac{\partial}{\partial x_j}\left(\bar{\rho}D_k\frac{\partial \tilde{Y}_k}{\partial x_j} - \overline{\rho u_j'' Y_k''}\right) + \dot{S}_{s.k} \tag{19}$$

The hybrid RANS/LES turbulence model is applied to the delayed detached eddy simulation (DDES) model proposed by Spalart [21] based on Menter's k-ω SST model [22]. The original k-ω SST model with Sarkar's compressibility modification [23] solves the turbulent kinetic energy and turbulent frequency for the conservative variable at each step. The source terms, $\dot{\rho}_s$, $\dot{F}_s$, $\dot{Q}_s$ and $\dot{S}_{s.k}$, represent the effects of the Lagrangian equation. In particular, the energy and species source terms account for the solid combustion. Each source term is calculated as

$$\begin{bmatrix} \dot{\rho}_s \\ \dot{F}_s \\ \dot{Q}_s \\ \dot{S}_{s.k} \end{bmatrix} = \frac{1}{V_{cell}} \begin{bmatrix} \dot{m}_{zpp.cell} \\ \dot{m}_{zpp.cell}u_p - \frac{\pi}{6}\rho d_{p.cell}^3 \frac{du_p}{dt} \\ \dot{q}_{zpp.cell} - h\pi d_p^2\left(T_g - T_p\right) \\ \dot{m}_{zpp.cell} \end{bmatrix} \tag{20}$$

The source terms are divided by cell volume, V_{cell}, because the terms are resolved-scale fractions. $\dot{m}_{zpp.cell}$ and $\dot{q}_{zpp.cell}$ represent the mass generation rate and energy gen-

eration rate of the total ZPP granules in a cell. A 5th order upwind WENO [24] scheme and a TVD 3-stage Runge-Kutta scheme are used forspatial discretization and temporal advancement, respectively. Multiple species with polynomial profiled specific heat, viscosity and conductivity are solved.

The dynamics of the dispersed particles are calculated using Newton's second law.

$$\frac{dx_p}{dt} = u_p \tag{21}$$

$$\frac{du_p}{dt} = \frac{F_p}{m_p} \tag{22}$$

where x_p, u_p and m_p represent the instantaneous particle location, velocity and mass, respectively. The force acting on the particle, F_d, is a drag force. it is given by

$$F_d = 1/8 \bullet C_d \rho \pi d_p^2 |u_r| u_r \tag{23}$$

Under the assumption of a perfect sphere, the criterion for the drag coefficient, C_d, can be presented as [25]

$$C_d = \begin{cases} 24/Re\left(1 + Re^{2/3}/6\right) & (Re < 1000) \\ 0.424 & (Re \geq 1000) \end{cases} \tag{24}$$

4 Prediction of the Valid Burning Surface Range Using 0-D Internal Ballistics

Figure 4 compares the experimental measurements and internal ballistics results as the granule diameter (burning surface) varies. The granule diameter is inversely proportional to the burning surface. The average diameter of the ZPP granules changes from 8.5 to 34 μm with an even amount of space to see the matching condition with the experiment. Because the combustion model is based on the sur-

face regression speed, the total burning time is directly related to the average diameter within the same pressure range. Note that the experimental results shift, and thus, the pressure ascent point starts at around 0.05 ms due to the pressure delivery time. This will be discussed in detail in the next chapter. Because the experimental measurements contain the pressure oscillation while the 0-D internal ballistics analysis represents the average pressure rise, an exact comparison of two results is unclear. However, the comparison does imply a valid range for the ZPP diameter that satisfies the combustion end time and overall behavior.
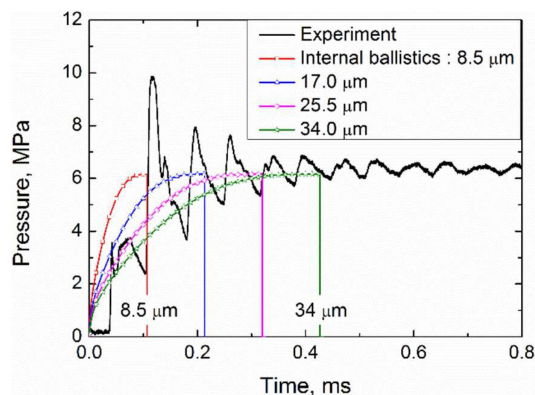
The experimental pressure curve has a weak first peak followed by the strongest second peak. After the second peak, the intensity weakens consistently. Two assumptions are suggested to describe this phenomenon. The first assumption is that the ZPP burns out after the second peak. In this case, there would be no heat or mass addition to the shock waves, and as such, the intensity of the shock wave would decrease because of the shock dissipation and heat loss. The second assumption is that the ZPP granules are evenly dispersed through the entire vessel. Because a shock wave propagates faster than ZPP granules, they would remain behind the shock waves during the first two peaks. However, the granules could subsequently disperse through the entire region while the pressure wave is reflected to the wall. Thus, the granules will finally exist across the pressure wave. In this case, the heat and mass generation in front of the wave will weaken the peak intensity. As such, the smallest possible average diameter of the ZPP granules is around 8.5 μm according to the first hypothesis and the largest is around 34 μm according to the second hypothesis. A specific determination is carried out below via a detailed CFD simulation.

5 CFD Simulation

5.1 Computational Domain

Figure 5 depicts a 2-D computational domain for a 10-cc cylindrical closed vessel. The diameter is 15 mm, and the height is 55.2 mm. A pressure cartridge is placed at the bottom of the domain. The number of particles to seed is calculated while taking volume similarity into account due to the 2-D simulation. Pressure data is integrated along the

Figure 4. Predicting the average granule diameter using 0-D internal ballistics.
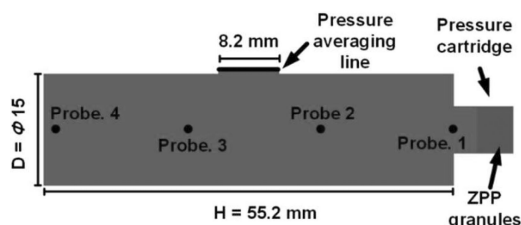
Figure 5. Computational domain of 10-cc cylindrical closed vessel.

pressure averaging line to facilitate a direct comparison with the sensor measurements. The line is located in the center with a step of 0.29 mm. Grids are fabricated in structured form with a total cell number of 235,000. The number of particles is between 100,000 and 200,000. All granules are assumed to ignite simultaneously at the beginning of a calculation. The initial condition has a temperature of 300 K, pressure of 1 atm and velocity of zero for both the gas and granules.

5.2 Flow Structures Inside the Vessel

Specific diameters are substituted to the CFD to confirm the adequate values based on the predicted granule diameter range according to the internal ballistics. Because CFD can predict the pressure oscillation, a direct comparison with the experimental measurements is conducted. Before proceeding, however, the physical phenomena inside the closed vessel, which cannot be observed experimentally, need to be analyzed.

Figure 6 depicts the contours of the particle distribution, pressure, temperature, density gradient and combustion products during the early pressure buildup process. The average ZPP diameter is 17 μm, and the loaded weight is 130 mg. The contours of the particle distributions show that the granules are driven by self-generated pressure, and they disperse into the domain. Most of the granules are consumed at around 0.15 ms. Pressure or density gradient contours imply that the rapid burning of the ZPP generates a strong shock wave. At 0.03 ms, when the first wave ascends, the pressure difference at the shock interface is around eight times. It increases consistently to around 15 times at 0.06 ms before the shock wave hits the wall. This occurs due to the continuous heat and mass addition from the granule combustion. After a reflection at 0.09 ms, the pressure difference becomes enormously large (more than 120 times) because the shock wave sweeps this region twice due to the reflection. The temperature and pressure behave similarly. This phenomenon is often exploited in closed end shock tube apparatuses to attain extremely high pressure conditions [26].

The granules slowly follow the shock wave and spread upward until the shock wave reaches the upper wall at around 0.06 ms. They only reach half of the vessel at 0.06 ms. The reflected shock wave advances downward and sweeps the granules forward. Because of the minus velocity behind the shock wave, the granules are pulled downward. Thus, most of the granules cannot reach the top wall. This implies that the calculation results are close to the first assumption in Chapter 4, which stated that the ZPP granules would burn out before the second peak. The leading edges of the combustion products exist between the leading edges of the granules and pressure. The combustion products dominate the gas properties, including the specific heat and gas constants. The superposition effect of the
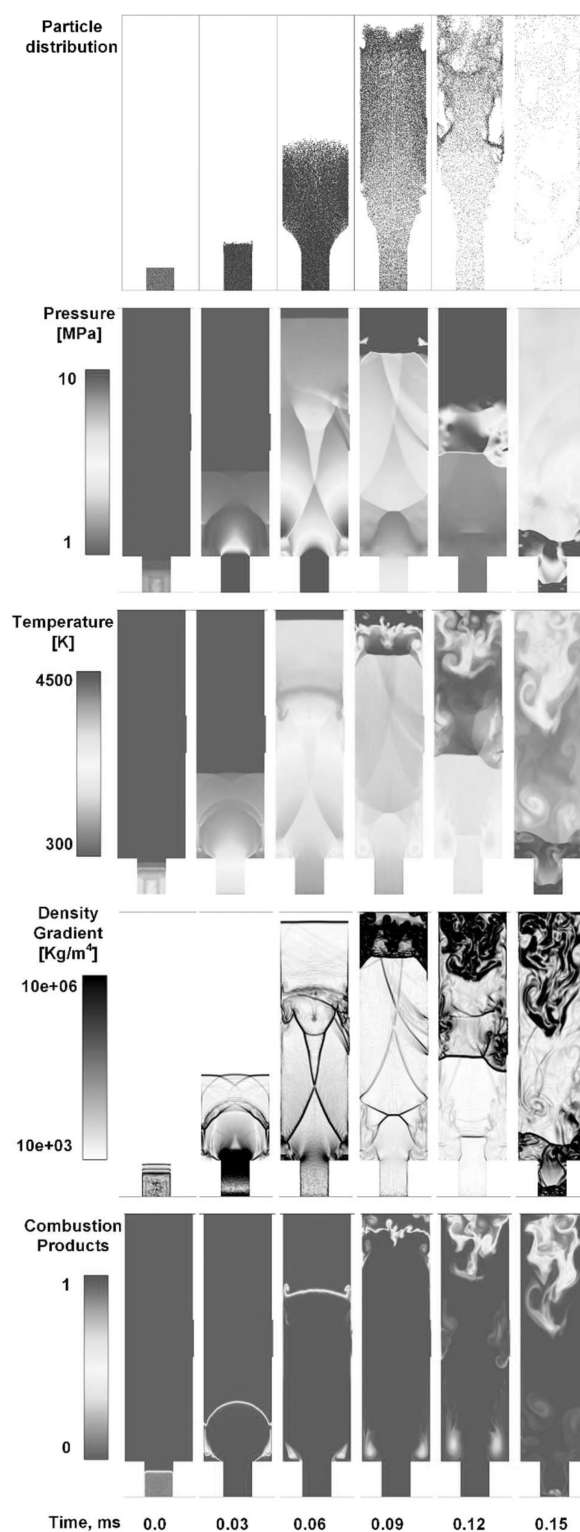

Figure 6. Contours of variables in early phases.

combustion products and shock wave had direct consequences on the temperature behavior.

The pressure data from the experimental and CFD results are obtained by averaging the area of the sensor plate. Therefore, the shock wave, which exhibits pressure discontinuity, directly affects the time-pressure histories, which will be discussed later. For instance, delays are caused by the time needed for the wave to travel from the pressure cartridge to the initial pressure ascent point, the pressure oscillation frequency and the intensity of each pressure peak, as seen in Figure 4.

These are important features when predicting and verifying the burn characteristics of the ZPP granules. Additionally, understanding these physics aids in the design similar experiments or devices. Appropriate sensors and positions can be determined for other experiments. A chamber shape that suppresses shock waves might minimize a pyrotechnic shock.

Figure 7 describes the pressure oscillation mechanism. Data is collected through a sensor plate, which is marked as a thick red line at the center right of the cylinder. In the figure, Min and Max denotes the pressure local minima and maxima, respectively. Positions 1, 2 and 3 show the weakening of the shock wave due to irregular reflection and separation. This occurs when the shock wave hits the bottom wall, which contains a cavity hole. The pressure-time curve indicates the local minimum when the shock wave arrives under the sensor tab (Position 1). Next, the pressure curve gently rises as a series of shock waves sweep the sensor tab (Positions 1 to 3). The pressure reaches its local maximum when the shock waves hit the top wall (Position 3). After this point, the waves unite and become a distinct strong shock wave, which begins to descend. The pressure gently decreases when the reflected shock descends (Positions 3 to 5). When the shock wave reaches the top of the sensor tab, the pressure becomes the local minimum again (Position 5). Unlike Positions 1 to 3, Positions 5 to 7 exhibit a single strong shock wave rather than a separation into a series of waves. Ther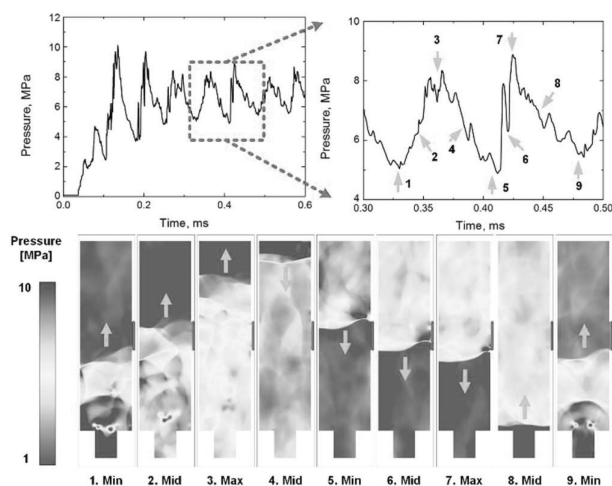efore, the pressure abruptly rises and becomes a local maximum when it reaches the bottom of the sensor tab (Positions 5 to 7). Because the front of the strong shock wave acts like a piston, the pressure behind the region of the shock decreases (Positions 7 to 9). This mechanism is repeated and generates a pressure oscillation.

5.3 ZPP Particle Size Effects

5.3.1 Monodisperse Distribution

The typical ZPP granule diameter is predicted by comparing the experimental data with the 0-D internal ballistics analysis. Figures 8 and 9 compare the results of the experimental data and CFD calculations using monodisperse assumption. 17- and 34-μm granule diameters are used for the simulations. Figure 8 reveals that the 17-μm diameter generally agrees well with the experiment. The amplitude and frequency of the first four peaks match well with the measurements. However, the calculated peaks shift slightly to the right compared to those of the measurements. The amplitude gradually decreases after the second peak due to the shock dissipation. However, the calculation overestimates the amplitude after the fourth peak. The calculation is 2-D-based, and it therefore neglects the 3-D effect. Thus, the simulation underestimates shock dissipation, and the amplitude of the shock is maintained. In addition, this might also be explained by the absence of the heat loss from the wall. After ignition (0 ms), a small pressure delay of about 0.04 ms is observed. This is the time required for the pressure to be delivered from the pressure cartridge to the sensor tab.
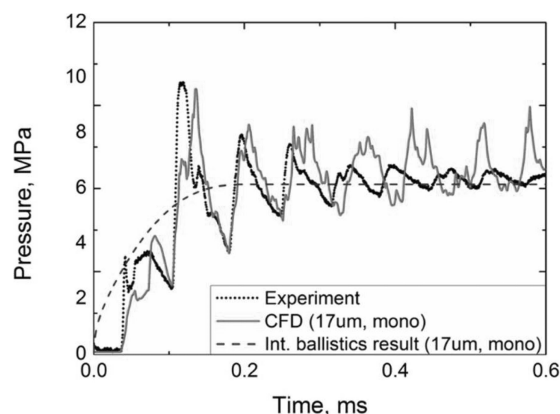

Figure 7. Pressure oscillation due to shock reflection.

Figure 8. Comparing the experiment, CFD and internal ballistics for the 17-μm monodisperse case.
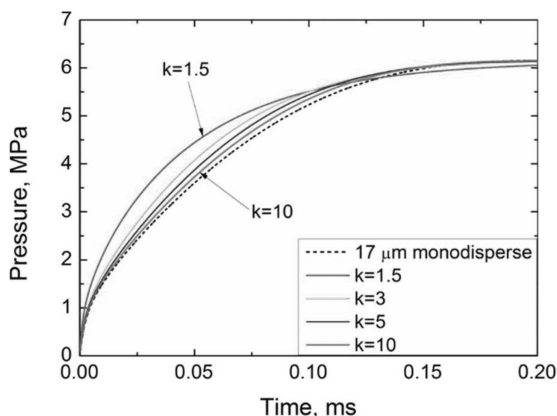
On the other hand, the pressure behavior exhibited by the 34-μm case is completely wrong. Meanwhile, the results of the internal ballistics adequately follow the peaks in the measurements, as shown in Figure 9. The overall pressure rises too gently with consistent amplitude. An abrupt pres-
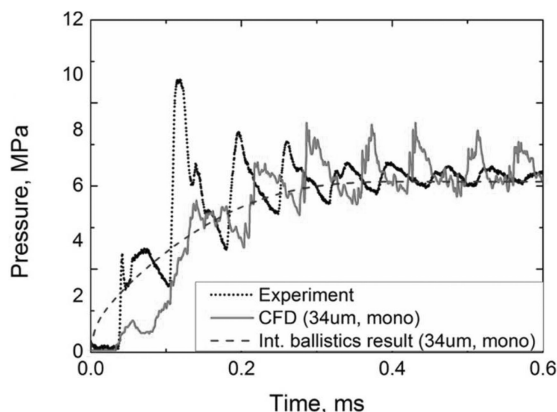
Figure 9. Comparing the experiment, CFD and internal ballistics in the 34-μm monodisperse case.

sure rise is absent at the beginning, as with the measurements in the 17-μm case. This occurs because the small burning area is not able to generate enough gas to form a strong shock wave right after ignition. Thus, the driving speed of the shock wave is slower than that of the 17-μm case, and each peak location shifts significantly to the right.

The effects of the initial granule size distribution are investigated. The CFD results under the monodisperse assumption show reasonable agreement to those of the measurements when the typical average diameter is 17 μm. However, in reality, the ZPP granules are not all the same size. Instead, they form a distribution. In this size distribution, many small granules generate hot gases rapidly and go extinct quickly, and vice versa for large granules. In this paper, the Rosin-Rammler equation is utilized to describe the size distribution. Figure 10 illustrates the initial seeding state of the ZPP granules under both the monodisperse and Rosin-Rammler distributions. The distributions are influenced by σ and k from Equation (7). Before adapt-

ing the Rosin-Rammler distribution to the CFD, its influence is tested using internal ballistics. The average diameter, σ, is fixed to 17 μm, and the distribution factor, k, varies from 1.5 to 10.

5.3.2 Rosin-Rammler Distribution

Figure 10 shows the internal ballistics results with the Rosin-Rammler distribution at σ = 17 μm and at different k values. All cases are compared to the 17-μm monodisperse case which shows reasonable agreement with the CFD results. A small k, which denotes a wide distribution, has a very stiff pressure-time curve at the beginning as small particles rapidly generate hot gases. However, its slope becomes gentle shortly thereafter as the small granules burn out. This results in a convergence toward the mono distribution as the k increases.

Figure 11 depicts the calculated gas generation rates at different k values. They are placed on the same graph with the experimental pressure curve so as to compare the timing of the ZPP combustion. Obviously, the maximum generation rate increases when k decreases. The maximum generation rate value is 850 mg/s when $k = 1.5$, while it is 490 mg/s in the 17-μm monodisperse case. This value affects the speed and intensity of the shock wave. All cases reach their peak before 0.05 ms.
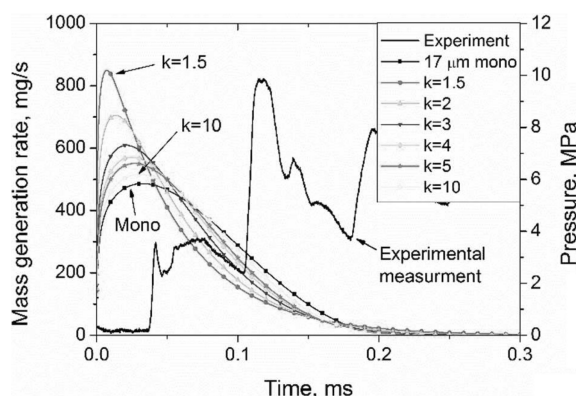

Figure 11. Mass generation rates at different k (σ = 17 μm) values compared to the measured pressure curve.

Figure 10. Internal ballistics with Rosin-Rammler distribution, σ = 17 μm.

In other words, the generation rate reaches its maximum and more than half of the ZPP is consumed before the first shock wave touches the sensor. This implies that the distribution will not change the pressure behavior dramatically over time, but it will be effective during the early transition phenomena. To observe the detailed differences according to the CFD, the following three cases are chosen: $k = 2$, 3 and 5.
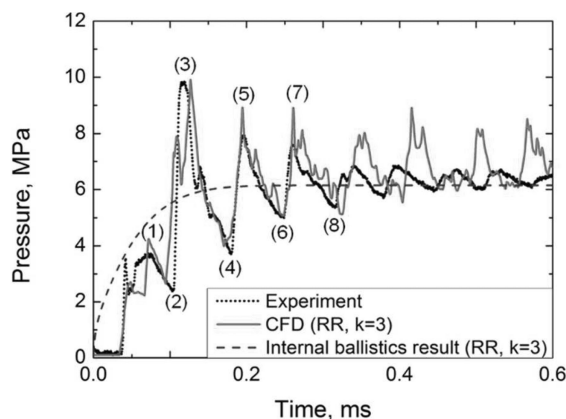
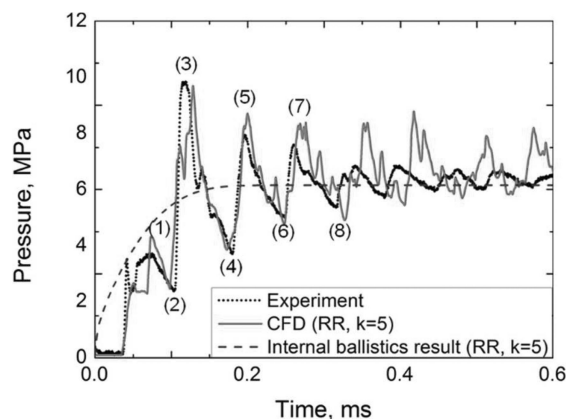Figure 12 displays the CFD results with a Rosin-Rammler distribution of σ = 17 μm and $k = 2$. The results are com-
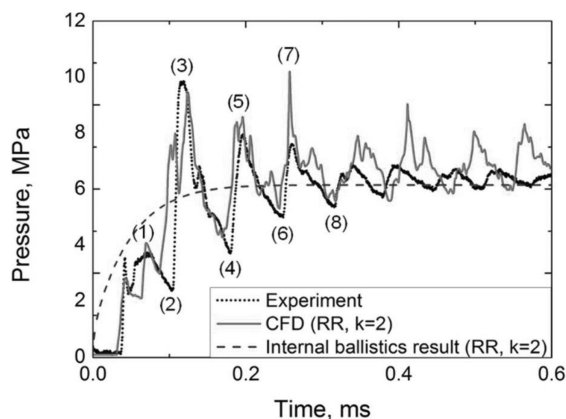
Figure 12. Comparison of pressure-time history of experiment, CFD and internal ballistics for the Rosin-Rammler distribution ($\sigma = 17\ \mu m$, $k = 2$).

pared with the internal ballistics in the same condition and with the experimental measurements. Comparing Figure 12 with Figure 8 (17-μm monodisperse), the upper peaks ((1), (3), (5) and (7)) agree reasonably well, whereas the peaks in Figure 8 shift. In addition, Figure 12 contains a stiffer slope at the beginning, unlike in the monodisperse case. However, the lower peaks ((2) and (4)), which agree well with the monodisperse case, become high and shift slightly to the left 1. Figure 13 is identical to Figure 12, except the k is 3. Because it has a narrow distribution and burn surface, the first rising slope is slightly more gradual than the $k = 2$ slope. Its lower peaks ((2), (4) and (6)) have better results compared to $k = 2$ while maintaining the accuracy of the upper peaks.

Figure 13. Comparison of pressure-time history of experiment, CFD and internal ballistics for the Rosin-Rammler distribution ($\sigma = 17\ \mu m$, $k = 3$).

Figure 14 represents the results for $k = 5$. It shows the best agreement with the measurements. The pressure curve

Figure 14. Comparison of pressure-time history of experiment, CFD and internal ballistics for the Rosin-Rammler distribution ($\sigma = 17\ \mu m$, $k = 5$).

after 0.3 ms still exhibits a high amplitude and long period compared with the measurements in all cases.

Figure 15 explains the above phenomenon. It displays the average shock speed under two different conditions. The line with squares shows the average shock speed between the point right after ignition and just before the shock reaches the sensor (when the shock is ascending). The line with circles shows the same information, but between the point after the first reflection and just before the shock reaches the sensor (when the shock is descending). The four cases are arrayed in order of burning surface. When the shock ascends after ignition, the average shock speeds are obviously almost proportional to the burning surface. When the shock descends after reflection, however, it is approximately constant for all distributions. The reason can be found by looking at the cumulative ZPP mass consumption, as indirectly shown in Figures 11 and 12. The descending shock speeds are averaged between 0.08 and 0.1 ms. At 0.1 ms, most of the ZPP is already consumed regardless of the distribution. Therefore, almost the same
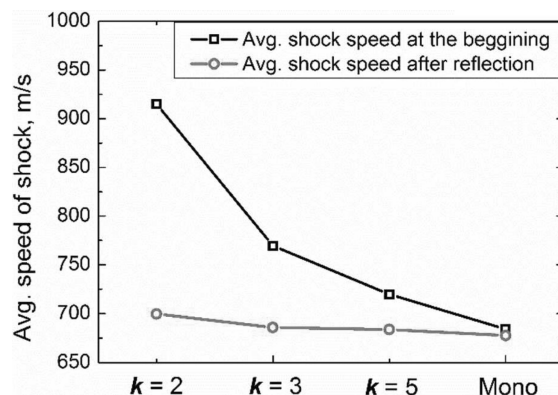
Figure 15. Average speed of shock after ignition, and the first reflection with respect to the granule distribution.

amount of combustion energy accumulates when the shock hits the upper wall and is reflected. Thus, the speeds of the descending shock become similar.

6 Conclusions

0-D internal ballistics and a 2-D two-phase numerical simulation are conducted to determine an adequate granule size and distribution. The reactive Eulerian-Lagrangian method is utilized for the ZPP combustion. A conventional closed vessel test ignites 130 mg of pressed ZPP inside a 10-cc cylindrical vessel and measures the pressure-time history. The result involves strong pressure oscillations. Therefore, the range roughly between 8.5 and 34 μm is specified as valid by comparing the 0-D internal ballistics and the measurements. On the other hand, the reactive two-phase CFD is able to simulate pressure oscillations to facilitate a comparison between the data and measurements in detail. When assuming granule monodisperse conditions, 17 μm represents a reasonable agreement with the measurements, while 34 μm indicates a lack of shock wave intensity. The detailed flow structure and granule behavior are observed. An intense shock wave is generated by the heat and mass discharges from the ZPP granule. The released shock is reflected and vibrates inside the vessel, which results in a pressure oscillation. In addition, the bottom cavity splits the shock, which affects the pressure measurements. Additionally, the Rosin-Rammler distribution is tested with respect to the distribution factor, k. In this work, $k = 2$, 3 and 5 are compared. A small k value exhibits a wide burning surface during the initial state and narrow burning surface later on. As the k value increases, the burning surface becomes analogous to that under monodisperse conditions. Therefore, $k = 2$ generates a fast and strong shock wave in the beginning, which shifts the pressure peaks to the left. According to the simulation, $k = 5$ provides the best match when compared to the monodisperse condition and other k values.

Nomenclature

δ_{ij}	Kronecker delta (Identify matrix)
η_{cp}	Mass ratio of condensed phase
ρ	Density
σ	Representative diameter of Rosin-Rammler equation
τ_{ij}	Deviatoric stress tensor
a	Burning constant
A_b	Total burning area of granules
b	Co-volume
c_p	Specific heat at constant pressure (total gas)
c_v	Specific heat at constant volume
C_d	Drag coefficient
d_p	Granule diameter
D_k	Destruction term of kinetic energy
E	Specific total energy

F_d	Force acting on a particle
$\dot{F}$	Source term of momentum
h	Convective heat transfer coefficient
h_{comb}	Combustion enthalpy of solid ZPP
k	Distribution factor of Rosin-Rammler equation
m	Mass
M_t	Total loaded mass of ZPP
M_{total}	Total gas mass in a current vessel
MW	Molecular weight
n	Burning exponent
N	Total number of granules
p	Pressure
$\dot{Q}_s$	Energy source term
q_j	Heat flux vector
Q_{loss}	Rate of energy loss
$\dot{q}_{zpp}$	Rate of energy discharge by ZPP combustion
R	Gas constant
Re	Reynolds number
$\dot{r}$	Regression rate
$\dot{S}_{s.k}$	Source Flux of Species k
T	Temperature
u	Gas velocity
V	Volume of closed vessel
$\dot{w}_k$	Mass Production of Species k
Y_i	Species mass fraction

Superscripts

•	Time difference
–	Time average
~	Favre average

Subscripts

ind	Individual species
l, j, k	Spatial coordinate index
mix	Mixed gas
avg	Average
cp	Condensed phase
p	Particle (granule)
g	Gas
r	Relative
cell	Cell
ZPP	Zirconium Potassium Perchlorate

Acknowledgements

References

[1] D. Han, H. Sung, S. Jang, B, Ryu, Parametric Analysis and Design Optimization of a Pyrotechnically Actuated Device, *Int. J. Aeronaut. Space* **2016**, *17*, 409–422.

[2] B. H. Paul, K. A. Gonthier, Analysis of Gas-Dynamics Effects in Explosively Actuated Valves, *J. Propul. Power* **2010**, *26*, 479–496.

[3] L. J. Bement, M. L. Schimmel, *A Manual for Pyrotechnic Design, Development and Qualification*, NA*SA-TM-110172,* NASA Langley Research Center, Hampton, VA, USA **1988**.

[4] L. J. Bement, *Pyrotechnic System Failures: Causes and Prevention*, NA*SA-TM-100633,* NASA Langley Research Center, Hampton, VA, USA **1988**.

[5] K. A. Gonthier, J. M. Power, Formulation, Predictions, and Sensitivity Analysis of a Pyrotechnically Actuated Pin Puller Model, *J. Propul. Power* **1994**, *10*, 501–507.

[6] S, Jang, H. Lee, J. Oh, Performance Modeling of a Pyrotechnically Actuated Pin Puller, *Int. J. Aeronaut. Space* **2014**, *15*, 102–111.

[7] H. S. Lee, Unsteady Gas Dynamics Effects in Pyrotechnic Actuators, *J. Spacecr. Rockets* **2004**, *41*, 877–886.

[8] G. A. Buttigieg, G. H. Paine, R. C. Hsiao, Shock Tube Effect Inside a Pyrotechnic Igniter, *Propellants, Explos., Pyrotech.* **2015**, *40*, 743–748.

[9] A. Bougamra, H. Lu, Determination of Pressure Profile During Closed-Vessel Test Through Computational Fluid Dynamics Simulation, *J. Therm. Sci. Eng. Appl.* **2016**, *8*, 021005-1-021005-5.

[10] K. Balakrishnan, S. Ukai, S. Menon, Clustering and Combustion of Dilute Aluminum Particle in a Post-Detonation Flow Field, *Proc. Combust. Inst.* **2011**, *33*, 2255–2263

[11] J. Corner, *Theory of the interior ballistics of guns*, John Wiley & Sons, New York **1950**, p. 85.

[12] M. A. Cooper, M. S. Oliver, The Burning Regimes and Conductive Burn Rates of Titanium Subhydride Potassium Perchlorate (TiH$_{1.65}$/KClO$_4$) in Hybrid Closed Bomb-strand Burner Experiments, *Combust. Flame* **2013**, *160*, 2619–2630.

[13] B. Ryu, J. Kim, J. Hwang, G. Ahn, Comparison of the Main Charge Characteristics for Pressure Cartridge, *41th KSPE Fall Conference*, Korea, 14–15 November, **2013**, *440–443*.

[14] W. K. Brown, K. H. Wohletz, Derivation of the Weibull Distribution Based on Physical Principle and its Connection to the Rosin-Rammler and Lognormal Distributions, *J. Appl. Phys.* **2016**, *17*, 409–422.

[15] L. C. Yang, Effects of Fuel Particle Size and Impurity on Solid-to-Solid Pyrotechnic Reaction Rate, *47th AIAA/ASME/SAE/ASEE Joint Propulsion Conference & Exhibit*, San Diego, CA, USA, 31 July - 03 August, **2011**, *AIAA 2011-5581*.

[16] B. L. Poulsen, K. K. Rink, Modeling the Energy Release and Burn Rate Characteristics of ZPP Based Initiators, *49th AIAA Aerospace Sciences Meeting including the New Horizons Forum and Aerospace Exposition*, Orlando, FL, USA, 4–7 January, **2011**, *AIAA 2011-271*.

[17] CEA, Chemical Equilibrium Application, **1994**, NASA Reference Publication 1311.

[18] National Institute of Standards and Technology, "NIST chemistry WebBook", **2016**, *(Online), Available:* http://webbook.nist.gov/chemistry/ [Accessed: 15-Feb-2017]

[19] I. A. Johnston, *The Noble-Abel Equation of State: Thermodynamic Derivations for Ballistics Modelling*, DSTO-TN-0670, Defence Science and Technology Organization, Edinburgh, Australia, **2005**

[20] D. Han, J. Shin, H. Sung, A detailed flame structure and burning velocity analysis of aluminium dust cloud combustion using the Eulerian-Lagrangian method, *Proc. Combust. Inst.* **2017**, *36*, 2299–2307

[21] P. R. Spalart, M. L. Shur, K. D. Squires, M. K. Strelets, A. K. Travin, A New Version of Detached-Eddy Simulation, Resistant to Ambiguous Grid Densities, *Theor. Comput. Fluid Dyn.* **2006**, *20*, 181–195

[22] F. R. Menter, Two-Equation Eddy-Viscosity Turbulence Models for Engineering Applications, *AIAA J.* **1994**, *32*, 1598–1605.

[23] S. Sakar, G. Erlebacher, M. Y. Hussaini, H. O. Kreiss, Analysis and Modeling of Dilatational Terms in Compressible Turbulence, *J. Fluid Mech.* **1991**, *227*, 473–493.

[24] G. S. Jian, C. W. Shu, Efficient Implementation of Weighted ENO Schemes, *J. Comput. Phys.* **1996**, 126, 202–228.

[25] F. M. White, *Viscous Fluid Flow 3rd edition*, McGraw-Hill, New York **2006**, p. 200.

[26] T. Bazyn, H, Krier, N. Glumac, Combustion of nanoaluminum at elevated pressure and temperature behind reflected shock waves, *Combust. Flame* **2006**, *145*, 703–713